Diamond & Related Materials 18 (2009) 433–437

Contents lists available at ScienceDirect

Diamond & Related Materials

journal homepage: www.elsevier.com/locate/diamond

Effects of nitrogen-doping on the microstructure, bonding and electrochemical activity of carbon nanotubes

Y.G. Lin [a], Y.K. Hsu [b], C.T. Wu [b], S.Y. Chen [a], K.H. Chen [b,c], L.C. Chen [c,*]

[a] Department of Materials Science and Engineering, National Chiao Tung University, Hsinchu 30010, Taiwan
[b] Institute of Atomic and Molecular Sciences, Academia Sinica, Taipei 10617, Taiwan
[c] Center for Condensed Matter Sciences, National Taiwan University, Taipei 10617, Taiwan

ARTICLE INFO

Available online 10 September 2008

Keywords:
Carbon nanotubes
Electron-transfer
Nitrogen-doping

ABSTRACT

Vertically aligned carbon nanotubes produced with in-situ doping of nitrogen (CN_x NTs) during chemical vapor deposition exhibit unique structural and electrochemical properties, which are strongly correlated with their nitrogen (N) doping level. In this work, the effects of N-doping on CN_x NTs have been systematically investigated via microstructure and bonding studies, electron-transfer (ET) behaviors, and subsequent electrochemical deposition of catalyst. The CN_x NTs doped with an optimal N level, while showing a nearly reversible ET behavior, in fact exhibit uniform and high density of surface defects. These surface defects are desirable for further modification and/or nucleation of catalytic particles on the surface of CN_x NTs to form a composite electrode for electrochemical energy device applications such as fuel cells and capacitors.

© 2008 Elsevier B.V. All rights reserved.

1. Introduction

Carbon nanoscience and nanotechnology have been developed very rapidly over the past decade since the discovery of carbon nanotubes (CNTs). Miniaturization of electronic and electrochemical (EC) devices using the single-walled CNTs has been demonstrated [1–3]. Meanwhile, the remarkable structure of CNTs offers attractive scaffolds for further anchoring of nanoparticles (NPs) and biomolecules, which is highly desirable for energy conversion/storage and molecular sensing applications [4–15]. For these applications, surface modification of the CNTs or attaching functional groups on the sidewall become a key issue. In particular, surface modification offers an opportunity to improve the EC reactivity of CNTs through facilitating an efficient route for their electron-transfer (ET) kinetics with ambient species or specific biomolecules. Therefore, understanding the ET behavior between the CNT surface structures and the active entities are essential.

Several approaches such as acid-based wet-chemical oxidation, amidation, or esterification, diimide activation and solubilization of CNTs have been adopted to effectively functionalize CNTs surface [16,17]. Despite that many solutions to modify CNTs are available, simple and reliable process to achieve such goal is still lacking. In the past we have introduced heteroatom dopant such as nitrogen (N) *in-situ* during the CNT growth and found it effective not only to change the atomic structure of the CNTs into bamboo like [18], but also to improve their electrochemical (EC) performance down the road [10]. Although many reports on nitrogen doped carbon nanotubes (CN_x NTs) are available in the literature [18–21], the role of N-doping in carbon nanotube and its resultant functionality is still not clearly understood.

In this paper, systematic studies on the effect of N incorporation in CNTs on the morphology, microstructures, electronic states, and electrochemical properties have been carried out. CN_x NTs with different nitrogen content have been produced using a simple *in-situ* nitrogen doping in a microwave plasma enhanced chemical vapor deposition (MPECVD) reactor [18]. Comparative studies to correlate the nitrogen content, microstructure, electronic structure, and EC performance of the CN_x NTs have been carried out. Subsequent loading of Pt NPs on the CN_x NTs to study the correlation of N doping with surface defect density and distribution has been carried out.

2. Experimental

For the synthesis of the CN_x NTs, an iron catalyst layer was deposited on Ti/Si substrates by ion beam sputtering prior to the NT growth step. Then CN_x NTs were grown on the precoated substrates by MPECVD method, which has been reported in our previous paper [18]. For Pt NPs deposition, a potential of −0.1 V vs Ag/AgCl in 0.5 M H_2SO_4 and 0.0025 M H_2PtCl_6 mixture solutions was performed for 15 s. Other details for the electrochemical deposition process are reported by Quinn and co-workers [22]. For microstructure and bonding investigation, a JEOL 6700 FESEM, HRTEM (JEOL-400 EX) and Microlab 350 XPS were used. Raman spectra were obtained with a Jobin Yivon Labram HR800 spectrometer with a 514.5 nm argon ion

* Corresponding author.
E-mail address: chenlc@ntu.edu.tw (L.C. Chen).

0925-9635/$ – see front matter © 2008 Elsevier B.V. All rights reserved.
doi:10.1016/j.diamond.2008.09.009

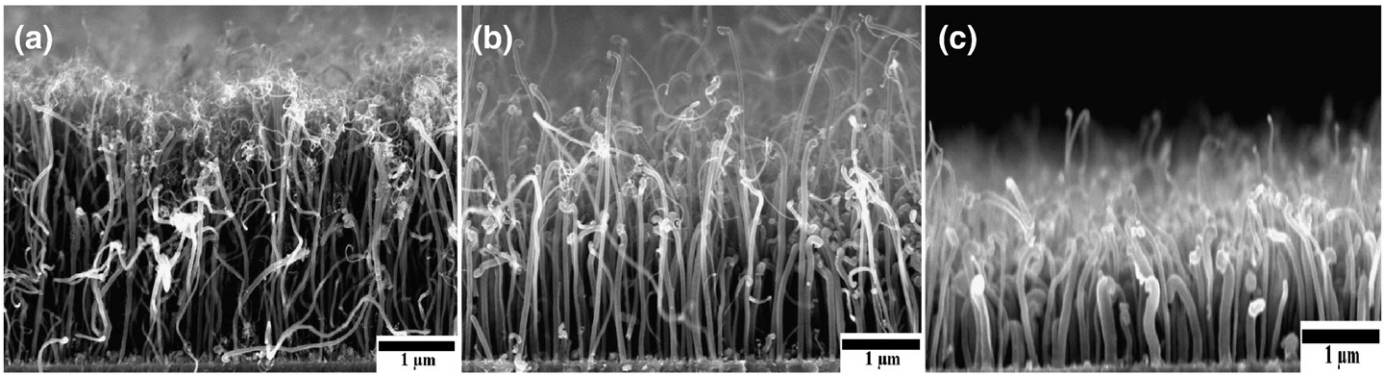

Fig. 1. Cross-sectional SEM images of the vertically aligned CNTs synthesized at different flow rate of N_2: (a) 0, (b) 80, and (c) 120 sccm.

laser. Cyclic voltammogram (CV) and AC impedance were recorded by using Solartron 1470E multichannel potentiostat system.

3. Results and discussion

3.1. Microstructure and bonding of nitrogen-doped carbon nanotubes

Fig. 1 shows the cross-sectional scanning electron microscopy (SEM) images of the vertically aligned CNTs synthesized using different flow rate of N_2 gas but otherwise identical growth parameters. The diameters of the CNTs thus produced are in the range of 20–50 nm with an approximate length of 2–4 μm. Bamboo-like structure of the CN_x NTs is observed, as reported in our previous paper [18]. However, as the N_2 gas flow is higher than 80 sccm the average diameter of the CNTs goes beyond 100 nm with a reduced length of 1–2 μm. This may be attributed to the higher growth temperature at higher N_2 flow rate, which is deviated from the nominal growth condition.

The Raman spectra of the CN_x NTs prepared under different nitrogen flow rate are presented in Fig. 2. The 1350 cm^{-1} peak (D band) in Fig. 2(a) corresponds to the disorder-induced feature due to the finite particle size effect or lattice distortion, while the 1580 cm^{-1} peak (G band) corresponds to the in-plane stretching vibration mode E_{2g} of single crystal graphite [23]. A D′ band around 1620 cm^{-1} at the shoulder of the G band is attributed to the symmetry breaking duo to the microscopic sp^2 crystallite size [24]. The D-band position and the ratio of the D- and G-band integrated intensities as a function of N_2 flow rate are depicted in Fig. 2(b) and (c), respectively. As the N_2 flow rate increases from 0 to 40 sccm the position of the D band up-shifts slightly and eventually down-shifts over 40 sccm nominal N_2 flow rate. In contrast, the position of the G band does not show clear dependence on the N_2 flow rate. Interestingly, the intensity ratio $I(D)/I(G)$ increases strongly as the N_2 flow rate is increased to 40 sccm and also decreases above the 40 sccm optimal flow rate. In principle, the $I(D)$ increases rapidly as a result of the enhanced defect density. Therefore, the up-shift of the D band and the

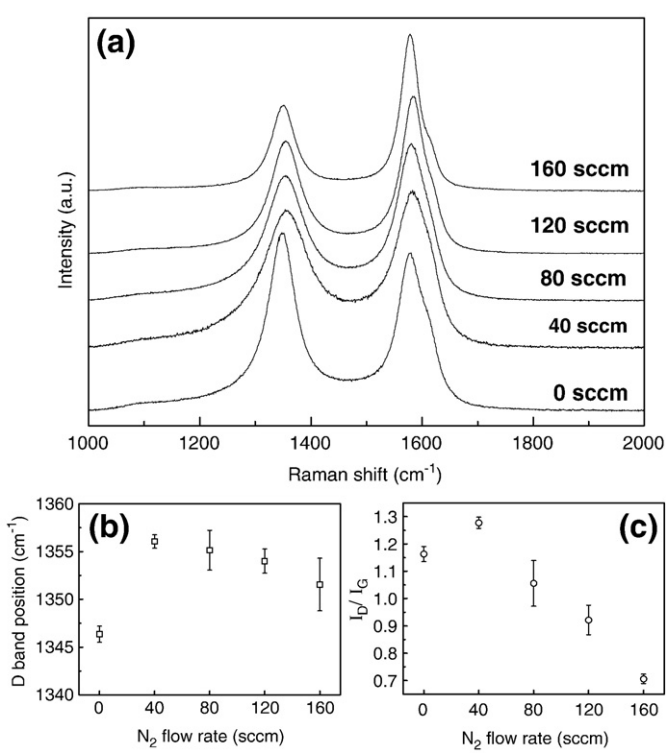

Fig. 2. (a) Comparison of the peak intensities and the full width at half maximum (FWHM) of the first-order Raman spectra for the vertically aligned CN_x NTs prepared with different N_2 flow rate during growth. (b) D-band position as a function of N_2 flow rate. (c) I_D/I_G as a function of N_2 flow rate.

increase in the ratio of the integrated intensities can be attributed to the increase of defect density in the graphitic structure and/or the enhancement of the edge plane by N-induced deformation in CN_x NTs. However, further increase of N_2 flow rate over 40 sccm leads to a higher growth temperature and results in enhanced graphitization degree. The growth temperature determined by pyroelectric thermal detector is 420, 450, and 750 °C at the N_2 flow rate of 0, 40, 160 sccm, respectively.

In order to obtain better understanding on the electronic structures of the CN_x NTs, X-ray photoemission spectroscopy (XPS) is applied to samples grown using different N_2 flow rates. Fig. 3(a) shows the C 1s spectra of the CN_x NTs after background subtraction using Shirley's method [25]. The C 1s spectra thus obtained can be decomposed into three Gaussian peaks including C1 peak at 284.4±0.1 eV representing the delocalized sp^2-hybridized carbon or graphite-like C–C bonding [26], C2 peak at 285.1±0.1 eV reflecting defect–containing sp^2-hybridized carbon associated with the trigonal phase with a sp^2 bonding [26,27], and the C3 peak at 290.5±0.5 eV originating from the CO-type bonding generated by the oxygen contamination of the CNTs exposed to the ambient air [26,28]. Detailed study of the peak position shows a slight up-shift from 0 to 40 sccm optimal N_2 flow rate followed by a down-shift at higher flow rate. This result is in agreement with the variation in the degree of structural disorder, which is associated with the electron density of the defect-containing sp^2-hybridized carbon and reflected in the FWHM of the C2 peak as illustrated in the inset of Fig. 3(a). The C2 FWHM reaches a maximum value at 40 sccm manifesting that the most pronounced disruption in the sp^2 carbon framework due to the incorporation of N atoms into the graphene lattice occurs at a N_2 flow rate of 40 sccm.

Likewise, the N 1s XPS spectra of the CN_x NTs with increasing N_2 flow rate are fitted by two Gaussian lines as shown in Fig. 3(b). The peaks at 398.1±0.2 eV (denoted by I_P) and 400.8±0.2 eV (I_G) are assigned to tetrahedral nitrogen bonded to a sp^3-hybridized carbon (so-called substitutional pyridine-like dopant structure) and trigonal nitrogen bonded to a sp^2-coordinated carbon (so-called substitutional graphite-like dopant structure), respectively [26]. Fig. 3(c) displays the fraction of pyridine-like and graphite-like defects as a function of the N_2 flow rate. Increasing N_2 flow rate is shown to give rise to an increase of the peak intensity ratios of the N-sp^3 C bonding (I_P), which is strongly related to graphene sheets. However, increasing N_2 flow rate, keeping the rest of the process parameters the same, also led to an increase in the reaction temperature. As a result, it is suggested the graphene sheets are easily buckled, facilitating the cross linking between the graphene planes through the sp^3-coordinated carbons. Meanwhile, the peak intensity ratios of the N-sp^2 C bonding decreases slightly over 40 sccm nominal N_2 flow rate. In general, N-doping is shown to lower the energy of pentagon defects in the graphite-like dopant structures. Thus, through the N-sp^2 C bonding, N atoms are easily incorporated in the graphene sheets. The total N-doping levels for the peak ratio of N/(N+C) are plotted against the respective N_2 flow rate in Fig. 3(d). The CN_x NTs with N_2 flow rate of 40 sccm contain maximum N atomic ratio.

3.2. Nitrogen-doping effect on electrochemical activity

The ET behavior of CN_x NTs are explored using a potassium ferrocyanide redox probe (5 mM $K_4Fe(CN)_6$ in 1 M KCl). A typical CV

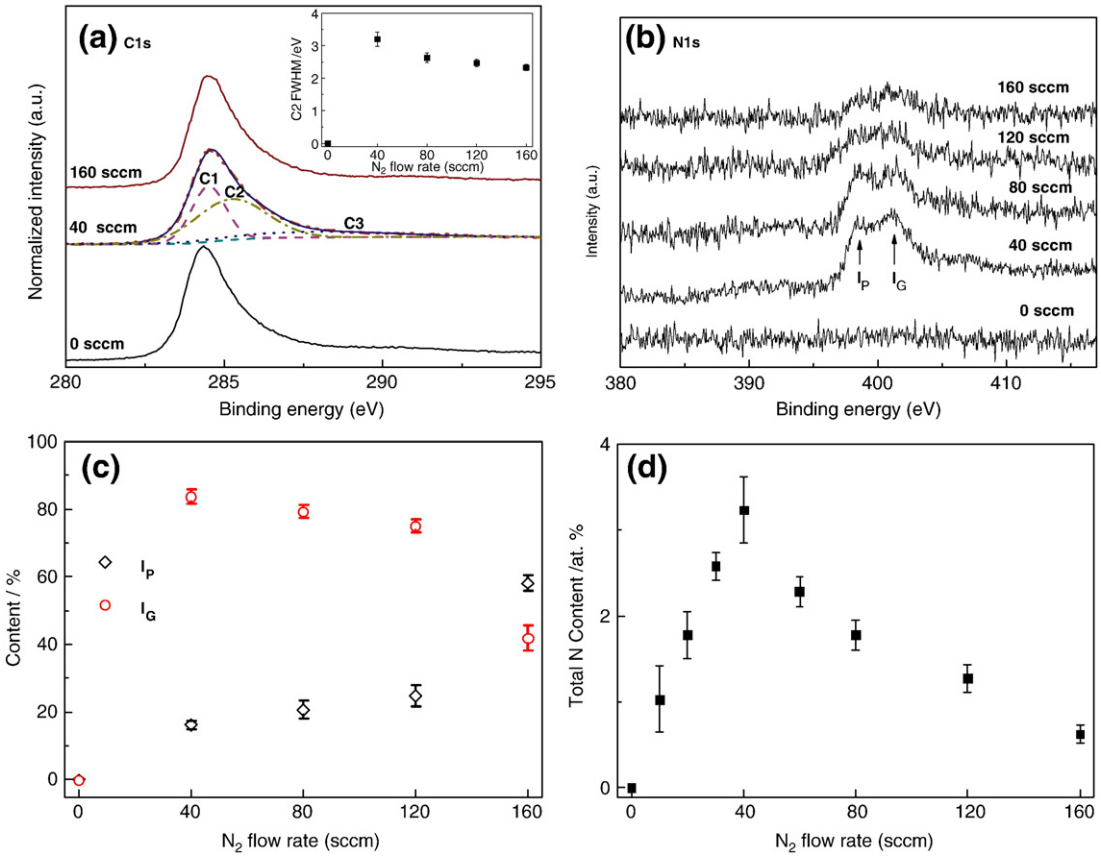

Fig. 3. (a) The C1s XPS spectra of the vertically aligned CNTs prepared with various N_2 flow rate during growth. The inset is the FWHM of the C–N bonding component as a function of N_2 flow rate. (b) The N1s XPS spectra of the vertically aligned CNTs prepared with different N_2 flow rate. (c) The I_P and I_G as a function of the N_2 flow rate for the N1s peak. (d) The N-doping concentration as a function of the N_2 flow rate.

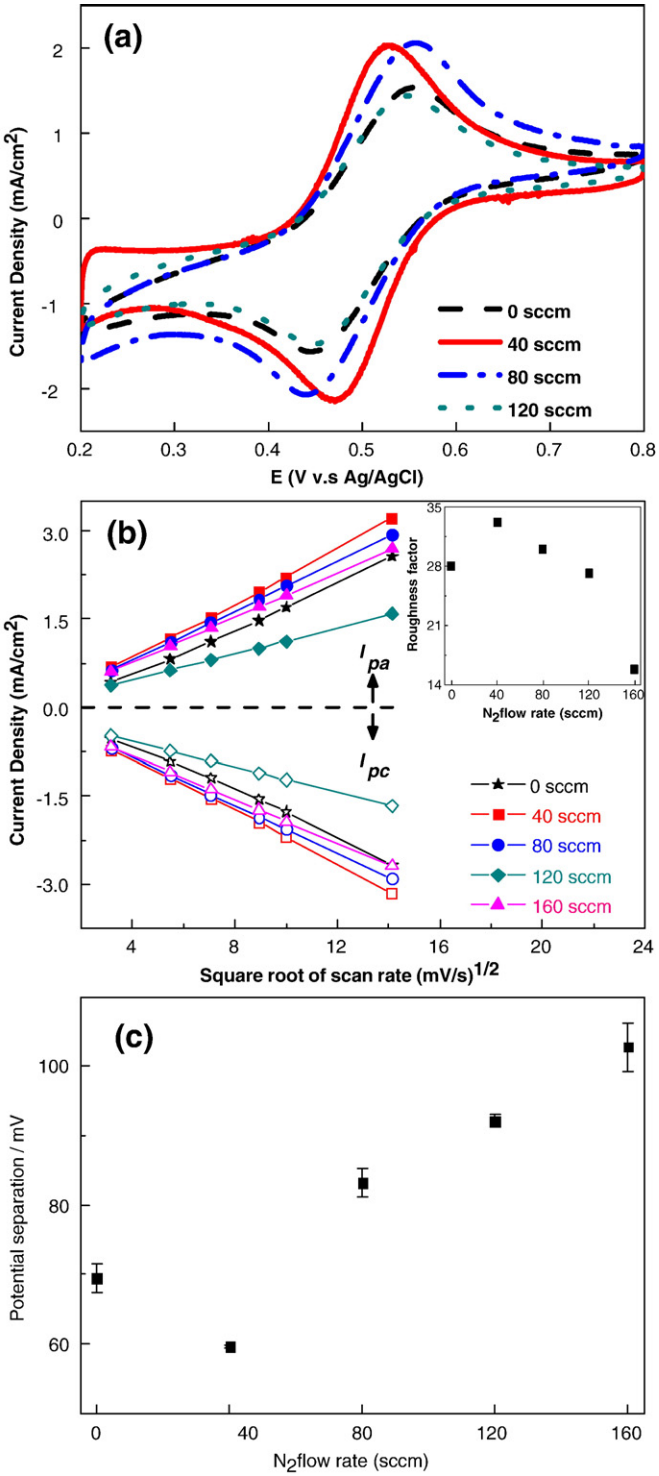

Fig. 4. (a) Cyclic voltammetry of the vertically well-aligned CNTs modified with different N-doping level in 1 M KCl and 5 mM $K_4Fe(CN)_6$. (b) The ferricyanide peak current versus the scan rate $(v)^{1/2}$ plot for CNTs using various flow rate of N_2 for both anode and cathode. (★: 0 sccm, ■: 40 sccm, ●: 80 sccm, ♦: 120 sccm, ▲: 160 sccm) The inset shows the roughness factor as a function of the N_2 flow rate. (c) The potential separation as a function of the N_2 flow rate.

curve of CN_x NTs microelectrode in this redox couple system is shown in Fig. 4(a). The well-defined peaks obtained in the forward and reverse scans are due to the Fe^{3+}/Fe^{2+} redox couple. The reversible redox reaction of the CN_x NT microelectrodes is further evidenced by the linear I_{pa} and I_{pc} vs $\upsilon^{1/2}$ plots shown in Fig. 4(b), where I_{pa}, I_{pc} and υ are the corresponding peak current densities of the cathodic and anodic reactions and the scan rate, respectively. These data indicate that the whole reactions are limited by semi-infinite linear diffusion of the reactants to the electrode surface. Moreover, the effective surface area of CN_x NT arrays can be evaluated from the slope of I_p vs $\upsilon^{1/2}$ based on Randles-Sevcik equation in the reversible redox system. The roughness factor, which is the ratio of the effective CN_x NTs surface to the geometrical electrode surface area, as a function of N_2 flow rate is depicted in the inset of Fig. 4(b). It is noted that the roughness factor of CN_x NT microelectrode prepared with N_2 flow rate of 40 sccm is ~33, showing significant enhancement in the effective surface area. Clearly, the N-doping induced electrochemically active sites on the surface of CN_x NT microelectrodes prepared with N_2 flow rate of 40 sccm are optimized.

The peak-to-peak separation (≥Ep) of potassium ferrocyanide redox probe is strongly dependent on the ET rate, namely, the reactivity of electrode materials to the electrolyte. In Fig. 4(c), ≥Ep of CN_x NTs with N_2 flow rate of 40 sccm is around 59 mV, reflecting excellent ET reactions. This is also related to the reduced internal resistance of the CN_x NT structures, which was determined by EC impedance (EIS) in 1 M KCl solution containing 5 mM $K_4Fe(CN)_6$ at an AC frequency varying from 0.1 to 100 kHz as shown in Fig. 5. From the point intersecting with the real axis in the range of high frequency, the internal resistance of the electrode is obtained. As shown in the inset of Fig. 5, the arrayed CN_x NTs microelectrode prepared with N_2 flow rate of 40 sccm shows the lowest resistance of all, which is in good agreement with the above mentioned measurements. Moreover, the Nyquist complex plane plot of the CN_x NT microelectrodes exhibits nearly straight line, which is characteristic of a diffusion-limiting step in the EC process, indicating that CN_x NTs possess better ET capability with selective N dopant.

The enhanced ET kinetics observed at CN_x NTs surface may in part be attributed to higher electronegativity of the CN_x NTs surface. The attractive interaction between the C–N dipoles present at the surface may attract the negatively charged members of the $Fe(CN)_6^{3-/4-}$ and accelerates the redox reactions. In fact, the rate constant for ET from the reactant to the electrode can be expressed as

$$k_{ox} = \int d\epsilon (1 - f(\epsilon, T)) w_{ox}(\epsilon),$$

where w_{ox} is the rate of ET from an occupied level of the reactant to an empty level of the electrode [29]. This ET rates are given in terms of the density of available states, the electron-resonance width and the strength of the coupling to the phonon bath [30,31]. The activation energy for the reaction decreases with increasing electronic interaction width. The structure of the NTs, as well as their local

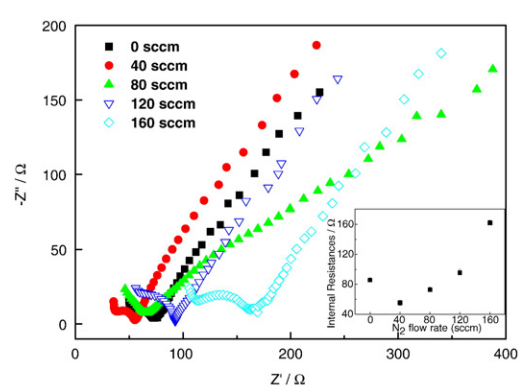

Fig. 5. AC impedance analysis of the vertically aligned CNTs with different N-doping level in 1 M KCl and 5 mM $K_4Fe(CN)_6$. The inset shows the internal resistance as a function of the N_2 flow rate.

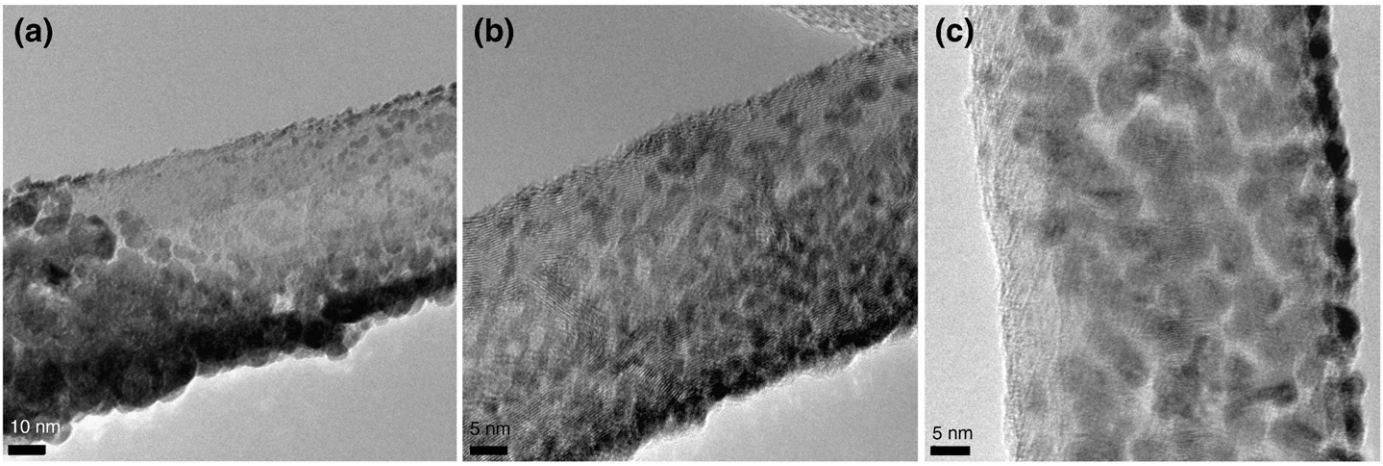

Fig. 6. TEM images of the Pt NP-CNx NT hybrid nanostructures synthesized at different flow rate of N_2: a) 0, b) 40, and c) 120 sccm.

density of states, might be responsible for the increase of the electronic-energy interaction width. In our case, arrayed CN_x NT microelectrode prepared with N_2 flow rate of 40 sccm has higher local-density of states (including surface defects induced states from XPS results), and promotes the enhanced ET kinetics.

The unique structures thus created in the *in-situ* N doping process can be verified by selective EC deposition technique, which is a direct and quantitative measure of the surface defects on individual CNTs. In this technique, a sequence of EC potentials were applied to the electrode, resulting in selective nucleation and deposition of metal at the chemical reactive sites such as the defect sites on CN_x NTs. Fig. 6 shows the comparative TEM images of the CN_x NTs prepared with various N_2 flow rate during growth and followed by 0.5 M H_2SO_4 and 0.0025 M H_2PtCl_6 mixture solutions. In Fig. 6(a) most of the Pt particles aggregate on the top of the electrode to form large agglomerates, indicating lack of nucleation sites on the side surface of CN_x NT prepared with no N_2 flow during growth. Fig. 6(b) shows more uniform and higher density of Pt NPs nucleating on the side surface of CN_x NTs prepared with 40 sccm N_2 flow rate during growth. However, excessive N_2 flow rate may cause adverse effect. Fig. 6(c) shows Pt agglomerates of tens of nanometers scattered throughout the CN_x NTs, which can be attributed to low nucleation density at this growth condition (120 sccm N_2 flow rate). Fig. 6(b) shows clear indication of the nearly monodisperse Pt NPs of 2–5 nm on the side surface of CN_x NTs having optimal defect density created under the 40 sccm N_2 flow rate during growth.

4. Conclusion

Vertically aligned CN_x NTs have been synthesized using microwave plasma enhanced chemical vapor deposition with different nitrogen flow rate. The microstructure, bonding and electrochemistry properties have been investigated utilizing Raman, XPS, CV and AC impedance measurements to establish correlations among the N content, electronic structure, microstructure and EC activities. The results show that nitrogen incorporation provides a simple pathway to engineering/modifying the microstructure and electronic bonding structure, which is crucial to the ET kinetics of the CN_x NT electrode. *In-situ* N doping of the CNTs at an optimal 3.5 at.% N is effective in converting the nanotubes into bamboo-type morphology and promoting substitutional graphite-like defect structure, which is favorable for fast ET in electrochemistry. The surface defects thus created further enhance anchoring of Pt atom in the subsequent selective EC deposition to produce ultrahigh density Pt NPs to form nanocomposite, which is ideal for many applications such as fuel cell electrocatalyst. Therefore, the *in-situ* N doping of CNTs provides a simple and effective technique to produce CNx NTs, which are highly desirable in many EC based applications.

Acknowledgement

This research was financially supported by the Asian Office of Aerospace Research and Development under AFOSR, National Science Council, National Taiwan University and Academia Sinica.

References

[1] S. Saito, Science 278 (1997) 77.
[2] G. Che, B.B. Lakshmi, E.R. Fisher, C.R. Martin, Nature 393 (1998) 346.
[3] S. Agrawal, M.J. Frederick, F. Lupo, P. Victor, O. Nalamasu, G. Ramanath, Adv. Funct. Mater. 15 (2005) 1922.
[4] A.A. Mamedov, N.A. Kotov, M. Prato, D.M. Guldi, J.P. Wicksted, A. Hirsch, Nat. Mater. 1 (2002) 190.
[5] A. Javey, Q. Wang, A. Ural, Y. Li, H. Dai, Nano Lett. 2 (2002) 929.
[6] A. Cao, R. Baskaran, M.J. Frederick, K. Turner, P.M. Ajayan, G. Ramanath, Adv. Mater. 15 (2003) 1105.
[7] K. Keren, R.S. Berman, E. Buchstab, U. Sivan, E. Braun, Science 302 (2003) 1380.
[8] N. Chopra, M. Majumder, B.J. Hinds, Adv. Funct. Mater. 15 (2005) 858.
[9] A. Gomathi, S.R.C. Vivekchand, A. Govindaraj, C.N.R. Rao, Adv. Mater. 17 (2005) 2757.
[10] C.L. Sun, L.C. Chen, M.C. Su, L.S. Hong, O. Chyan, C.Y. Hsu, K.H. Chen, T.F. Chang, L. Chang, Chem. Mater. 17 (2005) 3749.
[11] C.L. Sun, H.W. Wang, M. Hayashi, L.C. Chen, K.H. Chen, J. Am. Chem. Soc. 128 (2006) 8368.
[12] D. Shi, J. Lian, W. Wang, G. Liu, P. He, Z. Dong, L. Wang, R.C. Ewing, Adv. Mater. 18 (2006) 189.
[13] M.S. Raghuveer, A. Kumar, M.J. Frederick, G.P. Louie, P.G. Ganesan, G. Ramanath, Adv. Mater. 18 (2006) 547.
[14] C.H. Wang, H.Y. Du, Y.T. Tsai, C.P. Chen, C.J. Huang, L.C. Chen, K.H. Chen, H.C. Shih, J. Power Sources 171 (2007) 55.
[15] W.C. Fang, K.H. Chen, L.C. Chen, Nanotechnology 18 (2007) 485716.
[16] S.S. Wong, E. Joselevich, A.T. Woolley, C.L. Cheung, C.M. Lieber, Nature 394 (1998) 52.
[17] R.J. Chen, Y. Zhang, D. Wang, H. Dai, J. Am. Chem. Soc. 123 (2001) 3838.
[18] L.C. Chen, C.Y. Wen, C.H. Liang, W.K. Hong, K.J. Chen, H.C. Cheng, C.S. Shen, C.T. Wu, K.H. Chen, Adv. Funct. Mater. 12 (2002) 687.
[19] B.M. Klein, Nature 399 (1999) 108.
[20] J.C. Carrero-Sanchez, A.L. Elias, R. Mancilla, G. Arrellin, H. Terrones, J.P. Laclette, M. Terrones, Nano Lett. 6 (2006) 1609.
[21] G. Abbas, P. Papakonstantinou, G.R.S. Iyer, I.W. Kirkman, L.C. Chen, Phys. Rev. B 75 (2007) 195429.
[22] B.M. Quinn, C. Dekker, S.G. Lemay, J. Am. Chem. Soc. 127 (2005) 6146.
[23] D.G. McCulloch, S. Prawer, A. Hoffman, Phys. Rev. B 50 (1994) 5905.
[24] J. Kastner, T. Pichler, H. Kuzmany, S. Curran, W. Blau, D.N. Weldon, M. Delamesiere, S. Draper, H. Zandbergen, Chem. Phys. Lett. 221 (1994) 53.
[25] J.W. Jang, C.E. Lee, S.C. Lyu, T.J. Lee, C.J. Lee, Appl. Phys. Lett. 84 (2004) 2877.
[26] C. Ronning, H. Feldermann, R. Merk, H. Hofsass, Phys. Rev. B 58 (1998) 2207.
[27] J.P. Zhao, Z.Y. Chen, T. Yano, T. Ooie, M. Yoneda, J. Sakakibara, J. Appl. Phys. 89 (2001) 1634.
[28] H. Ago, T. Kugler, F. Cacialli, W.R. Salaneck, M.S.P. Shaffer, A.H. Windle, R.H. Friend, J. Phys. Chem. B 103 (1999) 8116.
[29] J.H. Mohr, W. Schmickler, Phys. Rev. Lett. 84 (2000) 1051.
[30] P.M. Ajayan, Chem. Rev. 99 (1999) 1787.
[31] J.F. Evans, T. Kuwana, Anal. Chem. 49 (1977) 1632.